Invited chapter to appear in the book, *Spectroscopy of transition-metal oxide interfaces*, Editors: C. Cancellieri and V.N. Strocov (Springer, in press).
Standing-Wave and Resonant Soft- and Hard- X-Ray Photoelectron Spectroscopy of Oxide Interfaces

Slavomir Nemšák [1], Alexander X. Gray[2] and Charles S. Fadley[3,4]

[1] Peter-Grünberg-Institut PGI-6, Forschungszentrum Jülich GmbH, 52425 Jülich, Germany

[2] Department of Physics, Temple University, Philadelphia PA 19122

[3] Department of Physics, University of California Davis, Davis, CA 95616 USA

[4] Materials Sciences Division, Lawrence Berkeley National Laboratory, Berkeley, CA 94720

Table of contents

Abstract

We discuss several new directions in photoemission that permit more quantitatively studying buried interfaces: going to higher energies in the multi-keV regime; using standing-wave excitation, created by reflection from either a multilayer heterostructure or atomic planes; tuning the photon energy to specific points near absorption resonances; and making use of near-total-reflection geometries. Applications to a variety of oxide and spintronic systems are discussed.

1 Basic principles of resonant standing-wave soft- and hard- x-ray photoemission (SXPS, HXPS) and angle-resolved photoemission (ARPES)

1.1 Standing-wave photoemission and resonant effects

In the chapters by Strocov, Cancellieri, and Mishchenko and by Sing and Claessen, the historical background, virtues and challenges of going upward from the typical limit in valence-band studies of ~150 eV into the soft x-ray (from a few hundred to ~2 keV) and hard (tender) x-ray regimes (~2-10 keV) in photoemission, including both core-level and valence-band angle-resolved photoemission (ARPES) measurements, have been discussed in detail, and we refer the reader to them, as well as to a prior overview article on ARPES by one of us [1], for background. There is also a recent book edited by Woicik that explores various aspect of hard x-ray photoemission [2]. We will use SXPS and HXPS (aka HAXPES) for these different energy regions.

In this chapter, we will add to these techniques the use of standing-wave (SW) excitation, resonant excitation to tune the SW properties, and the use of total reflection at buried interfaces to provide greatly enhanced resolution of buried interfaces, as well as bulk electronic structure. The SW method and its history is extensively discussed in various chapters in the book by Zegenhagen and Kazimirov [3].

SWs can be created by reflection from a synthetic multilayer, from atomic planes in single crystals or epitaxial overlayers, or in total reflection from buried interfaces. As photon energy is increased in these measurements, deeper interfaces or more truly bulk electronic structure can be studied. Prior reviews of these developments using multilayer reflection from our group provide additional background [4,5,6,7], including a detailed discussion of the x-ray optical theoretical modeling that is necessary to interpret experimental data [8].

Figure 1 illustrates the basic idea of SW photoemission. Strong Bragg reflection from either a multilayer heterostructure or atomic planes creates a standing wave inside of and above the sample. If the bilayer repeat spacing in a multilayer is d_{ML}, it is simple to show that, for first-order Bragg reflection, the standing wave period in $|E^2| \equiv \lambda_{SW} = d_{ML}$. The same is true in Bragg reflection from atomic planes with spacing $d_{hk\ell}$, where $\lambda_{SW} = d_{hk\ell}$. The relevant Bragg equations are $n\lambda_x = 2d_{ML}\sin\theta_{inc}$ and $n\lambda_x = 2d_{hk\ell}\sin\theta_{inc}$, where λ_x is the x-ray wavelength, n the order of the reflection, and θ_{inc} the angle of incidence relative to the multilayer or atomic planes. The SW can be scanned through the sample in one of three ways, as indicated: scanning the incidence angle θ_{inc} over the Bragg reflection through a rocking curve (RC), scanning photon energy $h\nu$ through the Bragg reflection, or tuning to the Bragg reflection and scanning the x-ray spot over a wedge profile sample grown on top of the mirror, which has been referred to as the SWEDGE method [9]. The first two scan the standing wave over half of its period; the wedge scan can involve multiple periods. From the basic SW formulas in Figure 1, in which R is the reflectivity, φ is the phase shift between incident and reflected waves, z is the relative "coherent" position of a given atom under SW excitation and f the fraction of atoms that occupy a given coherent position, we can see that the modulation of the SW field strength will be proportional to $\pm 2\sqrt{R}$. Thus, for

only a 1% reflectivity, one expects an overall 40% modulation in SW strength, making such measurements overall easier to perform than might at first sight be imagined.

An added interference effect often seen in such measurements is Kiessig (or Fresnel) fringes, which are associated with the x-ray reflection from the top layer(s) of a multilayer sample, and that from the bottom of it, where it meets the semi-infinite substrate on which the multilayer was grown. If the total thickness of the multilayer structure is D_{ML} then these interference peaks are described by $m\lambda_x = 2D_{ML}sin\theta_{inc}$, with much smaller angular separation than the Bragg peaks. These will be evident in some of the data discussed below, and are schematically illustrated in Figure 2(a).

As an additional aspect of such SW studies, tuning the photon energy to somewhere near a resonance can enhance reflectivity significantly, as done by Gray et al. in a study of the $SrTiO_3/La_{0.7}Sr_{0.3}MnO_3$ interface in a multilayer sample [10]; here, the energy was tuned to just below the La M_5 resonance, with a resultant three-fold increase in reflectivity from off-resonance, or an $\sim\sqrt{3}$ increase in the SW modulation, as illustrated in Figure 2. Figure 2(a) shows the sample configuration, with various quantities defined. In Figure 2(b) is shown the La M_5 absorption spectrum, and in Figure 2(c) the reflectivity in first-order Bragg reflection for various photon energies over the resonance. The presence of Kiessig fringes is also indicated in Figure 2(c).

A second possibility for tuning the SW is shown in Figure 3. Figure 3(a) shows a plot of the real and imaginary parts of the index of refraction (δ and $\beta \propto$ absorption, respectively) of Gd over its analogous M_5 resonance, and Figures 3(b) and 3(c) the variation of the calculated electric field strength $|E^2|$ as a function of depth and incidence angle for a similar $SrTiO_3/GdTiO_3$ multilayer [11]. From the energy position just below the resonance at 1181 eV (Figure 3(b)) to one about the same distance above it at 1187 eV (Figure 3(c)), the position of the SW maximum at the Bragg reflection moves from a position near the top of the $SrTiO_3$ layer to a position near the $SrTiO_3/GdTiO_3$ interface. This effect was first pointed out in Bragg reflection from crystal planes [12], and has been used by Nemšák et al. in a recent SW study of a two-dimensional electron gas (2DEG) near the interface in this system [11], as discussed below.

Thus, reflectivity and the SW modulation amplitude, as well as the SW vertical position, can be tuned by selecting photon energies at appropriate positions below or above a strong absorption maximum, providing capabilities that we will illustrate in example applications below.

1.2 Near-total reflection measurements

Total reflection in SXPS at ~1 keV was first studied in detail by Henke [13], who pointed out the decreased depth of x-ray penetration for low incidence angles, and the existence of an enhanced peak in intensity just before total reflection. This was pointed out as a technique for surface analysis by Mehta and Fadley [14] and later amplified for this purpose by Jach and co-workers [15] and by Kawai et al. [16], including a recent comprehensive review [17]. Interference fringes in near-total-reflection (NTR) from overlayers on thick substrates have also been pointed out [17]; these in effect consist of standing waves of varying periods as θ_{inc} is scanned into total reflection. The use of such NTR effects to characterize the different depths in multilayer structures has also been discussed, e.g. in ref. 8, discussion of Figure 17. We return below to making use of NTR measurements to study charge accumulation at a buried oxide interface [18].

1.3 ARPES in the soft- and hard- x-ray regimes

As discussed in the chapter by Strocov, Cancellieri, and Mishchenko, extending such measurements into the soft and hard x-ray regimes requires considering both the effects of phonon excitation during photoemission, which can smear the momentum resolution in ARPES measurements, and lattice recoil, which can shift and smear the energy resolution in any sort of spectrum.

The effects of phonon excitation in reducing the fraction of simply-interpretable direct transitions (DTs) can be estimated from a photoemission Debye-Waller factor,

$$W(T) \approx exp[-g_{hk\ell}^2 \langle u^2(T) \rangle], \quad [1]$$

with $g_{hk\ell}$ the magnitude of the reciprocal lattice vector involved in a given direct transition (DT) and $u^2(T)$ the one-dimensional mean-squared vibrational displacement at temperature T.

As an illustration of how important these effects might be, Figure 4(a) shows a plot of the photon energy for which 50% of the transitions remain direct at 20K (a reasonable criterion for being able to carry out ARPES), as a function of the two relevant parameters of Debye temperature and atomic mass, with points for various elements indicated [19]. These are calculated using the Debye model. This plot can be used to estimate the feasibility of a given ARPES experiment as energy is increased, although prior experiments make it clear that such simple estimates can be on the conservative side. One likely reason for this is that the Debye model does not include correlation of vibrations for near-neighbor atoms, that is, that nearest and next-nearest neighbor atoms will vibrate less than atoms further away, being more rigid in their motion with respect to a given atom [20]. A more accurate method of modeling such phonon effects has been developed by Braun et al. [21]; this makes use of the coherent potential approximation (CPA) to model the effects of atomic displacements, and is the first quantitative modeling of the temperature dependence of soft- and hard- x-ray ARPES.

Recoil can also be estimated by assuming a single-atom of mass M recoils in the lattice, again a conservative estimate, which yields the energy shift as

$$E_{recoil} \approx \frac{h\nu}{2M} \approx 5.5 \times 10^{-4} \left[\frac{E_{kin}(eV)}{M(amu)} \right]. \quad [2]$$

Figure 4(b) shows a family of curves of recoil energy, as a function of photon energy and mass, again permitting an estimate of the shifting and smearing expected for a given system. Of course, such recoil effects are most significant for lighter elements, but they also depend crucially on the Debye temperature, or more precisely the rigidity of the vibrational potentials associated with a given atom. The Debye-Waller factor in Equation 1 can in fact be used to estimate the fraction of transitions that occur with no recoil, in the same spirit as in the analysis of Mössbauer spectra. But different local correlated vibrational environments for different atoms will no doubt lead to deviations from the simple estimates of Figure 4. For example, Figure 4(b) notes that the Debye temperature for in-plane vibrations in graphite, or equivalently in graphene, is much higher than that perpendicular-to-plane. Thus ARPES for graphite/graphene connected with in-plane dispersions is expected to be possible at much higher photon energies (ca. 2000 eV from the figure) and/or temperatures. The two plots in Figure 4 are highlighted for W and GaAs, the two materials for which it was first demonstrated by Gray et al. [22] that ARPES could be performed at up to 6 keV and 3 keV, respectively.

Finally, we note that, in the limit of high photon energies and/or high temperatures and/or a high angular integration in the electron spectrometer, VB spectra converge to what can to a first approximation be considered as a matrix-element-weighted density of states (MEWDOS) limit, or more simply, what has often been referred to as the "XPS limit".

2 Applications to various oxide systems and spintronics materials

2.1 Overview of past studies - standing waves from multilayer reflection

Standing-wave spectroscopy from multilayer samples began with work by Bedzyk et al. [23] using x-ray fluorescence detection, by Kortright et al. [24,25] using x-ray magnetic circular dichroism, and by our collaborators using photoemission [26]. These studies have by now involved sample which have been grown as the multilayer or on top of a suitable multilayer, with applications to a wide range of materials systems, some of which we list below, before focusing on some much more recent studies that demonstrate the full potential of the technique:

- **The Fe/Cr giant magnetoresistive interface:** The interface depth profiles of concentration and magnetic order were determined, the latter being via photoemission magnetic circular dichroism (PMCD) measurements [9]. This study made use of the standing-wave wedge (SWEDGE) method illustrated in Figure 1.
- **A CoFeB/CoFe/Al_2O_3 magnetic tunnel junction:** The depth-dependent variation of the buried-layer density of states was determined, and related to tunneling properties [27].
- **Co microdots on a silicon substrate:** The use of scanned-photon-energy SW excitation to add depth resolution in photoelectron microscopy was demonstrated [28].
- **The Fe/MgO magnetic tunnel junction system:** The variations of atomic concentrations, densities of state, and Fe magnetization through the interface were determined, again using PMCD and the SWEDGE method [29].
- **The Ta/CoFeB/MgO magnetic tunnel junction system:** The diffusion of B with annealing of a Ta/CoFeB/MgO magnetic tunnel junction was determined with standing-wave hard x-ray photoemission [30].

2.2 Overview of past studies - standing waves from atomic-plane reflection:

Standing-wave spectroscopy with Bragg reflection from atomic planes has a longer history, with first measurements again involving x-ray fluorescence detection [31,32], and photoemission detection coming some time later [33].

A significant additional development involving atomic-plane Bragg reflection, of which we will make use below, is the combination of core-level rocking curve or energy-scan measurements with analogous valence-band (VB) data to decompose the VB data into element-specific components, as pioneered by Woicik et al. [34,35]. This will be discussed in more detail below.

2.3 Multilayer standing-wave soft- and hard- x-ray photoemission and ARPES from the interface between a half-metallic ferromagnet and a band insulator: $La_{0.67}Sr_{0.33}MnO_3/SrTiO_3$

In a combined soft x-ray/hard x-ray study using standing-wave excitation from a multilayer of $SrTiO_3$ (STO) and $La_{0.7}Sr_{0.3}MnO_3$ (LSMO), Gray et al. [10,36] demonstrated the power of the SW approach for determining the depth profiles of concentration, chemical state and valence-band electronic structure through buried interfaces. Some of these results are summarized in Figures 5-8. Figure 2(a) shows the sample configuration, and 2(b)-(c) the method of tuning the photon energy to maximize the SW strength. The photon energy 833.2 eV just below the La M_5 edge was chosen to maximize reflectivity and thus the SW modulation. Figure 5(a) illustrates the excellent theoretical fit to core-level rocking-curve results at 833 eV and 5.96 keV for all of the elements in the sample, Figure 5(b) the resulting depth distribution of bilayer thickness, and Figure 5(c) the depth distribution of concentration and soft x-ray optical constants. Of particular note is that the bilayer thickness drifted by ca. 6% over the 48-bilayer thickness, a finding confirmed later by TEM/EELS measurements. TEM/EELS also confirmed the findings in Figure 5(c), although it is not sensitive to a change in the soft x-ray optical constants of LSMO near the interface that are revealed by the SW photoemission analysis. Note also in Figure 5(b) that the rocking curves show features due to both the 1st-order Bragg reflection from the multilayer and Kiessig interference oscillations due to x-ray reflection from the top and bottom of the multilayer, with these being much stronger compared to the Bragg peak with hard x-ray excitation at ~6 keV. A likely explanation for this is that the higher-energy photons can more readily penetrate the full multilayer and reflect back from the substrate interface. Beyond this, Bragg reflection has been enhanced in the soft x-ray data by tuning the photon energy, as shown in Figure 2(b), and this may be another cause of the higher relative intensity of the Kiessig fringes at higher energy, where no resonance is involved.

Figure 6 further shows the detailed interface-sensitive SW core-level spectroscopy that is possible, with Mn 3*p*, but not Mn 3*s*, showing a small shift

near the interface. Figure 6(a) shows the variation in binding energy of Mn 3*p*, Ti 3*p*, and Mn 3*s* as angle is scanned over the Bragg condition. Only Mn 3*p* shows a small, but reproducible shift, as further seen in Figures 6(b) and 6(c). Figure 6(d) shows calculations of the wave field as a function of angle, verifying that Mn 3*p* shifts to higher binding energy by about 0.3 eV when the SW selectively probes the interface. These results have been explained in terms of an Anderson Impurity Model as being due to a Jahn-Teller distortion of the MnO_6 octahedra near the interface that does not affect Mn 3*s* or its well-known multiplet splitting (also shown in Figure 6(c)).

Figure 7 illustrates another groundbreaking aspect of these studies by Gray et al. [36] in which SW ARPES (SWARPES) measurements were made on the same system at two different angles of incidence to selectively look into the "bulk" of LSMO and at the LSMO/STO interface. Figure 7(a) shows the angle-integrated ARPES spectra, which should represent a matrix-element weighted density of states, with different regions labelled as to their origins: 1 strongly Mn e_g , 2 strongly Mn t_{2g}, 3 and 4 strongly STO states (due to its being the top layer of the sample), and 5 probably the lowest bands in LSMO. Figures 7(b), 7(c),and 7(d) are k_x-k_y SWARPES maps for enhanced "bulk" LSMO sensitivity, enhanced interface sensitivity, and the difference between the two, respectively. With the difference, one is able to selectively look at how the ***k***-resolved interface electronic structure differs from that further into the LSMO. Particularly for region 5, but also for the LSMO Mn 3*d* regions 1 and 2, there are significant differences that indicate these data represent the first time that ***k***-resolved changes in electronic structure near an interface have been measured. Theoretical calculations shown elsewhere, including using the most accurate one-step time-reversed LEED approach, are at least qualitatively in agreement with these data [36].

The work discussed in this section thus indicates the high sensitivity of SW soft- and hard- x-ray photoemission to the bonding configuration of atoms at interfaces, to the detailed character of the multilayer, including the depth distributions of all species and the index of refraction, and via SWARPES to the momentum-resolved electronic structure at the interfaces.

2.4 Multilayer standing-wave soft- and hard- x-ray photoemission and ARPES study of the two-dimensional electron gas at the interface between a Mott insulator and a band insulator: $GdTiO_3/SrTiO_3$

As a further illustration of the power of standing-wave photoemission, we show soft x-ray data for a $SrTiO_3/GdTiO_3$ (STO/GTO) multilayer in Figure 8. The STO/GTO interface is known from work by Stemmer et al. [37] to exhibit a two-dimensional electron gas (2DEG) for certain thicknesses of GTO sandwiched between STO. So a key question is whether the 2DEG can clearly be seen in soft x-ray ARPES using SW excitation, and whether its depth distribution can be directly measured. Figure 8(a) shows the multilayer sample we have studied, carrying out rocking curve measurements to vary the SW position. Figure 8(b) shows ARPES data at a Ti 2*p*-3*d* resonant energy of ~465 eV, and we see two features near E_F, one at about 0.7 eV binding energy that can tentatively be identified as the lower Hubbard band (LHB), and one at about 0.2 eV and extending to E_F that was tentatively identified as the 2DEG, with dispersion in k_x-k_y that is characteristic of such states. The panels A through E here represent different energy intervals over which the ARPES images were taken. The dispersive features are only seen clearly on resonance and so both must have a strong Ti 3*d* makeup; all of the panels also have very similar dispersion curves, suggesting strong admixing in character that is confirmed by hybrid-functional LDA calculations by Van de Walle et al. [11].

But is the 2DEG really at the interface, or can it be at the surface of the sample, perhaps arising in the final STO layer, as has been observed in low-energy VUV ARPES [38,39]. This is easily resolved by measuring rocking curves with incident energies of 1181 and 1187 eV just below and just above the Gd M_5 edge. From Figure 2, the x-ray optical calculations tell us that 1187 eV should result in a SW position centered on the interface, and Figure 8(c) shows these rocking curve

(RC) results at that energy. By comparing theoretical and experimental core-level curves from elements in different layers with the curves from what we assign to the 2DEG state, we can very clearly see that this state is localized near the buried STO/GTO interface, and that it extends through the entire STO layer. For example, the 2DEG RC is very different from that of C 1*s* (a surface impurity on top of the last STO layer) and from that of Gd 4*f* that arises over the bulk of the GTO layer, but it is essentially identical to the Sr 3*d* RC. Thus, we can conclude that the 2DEG is localized in STO near the buried interface and not at the surface, and that it is not a surface-specific 2DEG as seen previously with VUV ARPES [38,39]. Further comparing the experimental RC in Figure 8(c)-right panel with theoretical RCs for the 2DEG assuming it exists throughout the full STO layer and one assuming it exists within only the first unit cell above the interface (Figure 8(c)-left panel) confirms that the 2DEG essentially extends through the entire STO layer, consistent with prior resonant tunneling measurements [37]. The RC of the peak that we tentatively assigned to the GTO lower Hubbard band is very similar to that Gd 4f RC, thus confirming this assignment. Additional experimental and theoretical RC results of this type at 1181 eV confirm these conclusions [11].

Finally, Figure 8(d) compares a binding energy-k_x resonant ARPES plot with theoretical calculations based on hybrid functionals [11], and there is good agreement as to the general features. Theory also confirms our assignment of the LHB and the 2DEG.

These results thus constitute an illustrative example of what can be done for many oxide systems by mixing different resonant effects: standard resonant photoemission to enhance a given atom's contributions to soft x-ray ARPES, tuning to a resonant energy to maximize reflectivity and thus SW effects, and tuning above or below a given resonance to move the position of the SW more dramatically.

2.5 Multilayer standing-wave photoemission determination of the depth distributions at a liquid/solid interface: aqueous NaOH and CsOH on Fe_2O_3

Very recently, the possibility of using SW ambient pressure photoemission (SWAPPS) to directly study the sub-nm interface region near a solid/gas or solid/liquid interface has been demonstrated [40]. This region is critical to any surface reaction, catalytic reaction, or electrochemical process, and so is of high importance in many areas of environmental and energy research. For example, the electrochemical double-layer has been studied for over 100 years, and is not yet understood [41,42].

We illustrate this method with this first SWAPPS data for water reacting with NaOH and CsOH on the surface of a thin film of Fe_2O_3 grown on a Si/Mo multilayer mirror, at a pressure and temperature for which the surface can be considered to be "wet", with a thin film of "liquid-like" water on the surface [40]. Figure 9(a) shows the sample configuration, with excitation at 910 eV, and a solution of NaOH and CsOH that was prepared by drop casting onto Fe_2O_3 in air and then inserting into a "humid" vacuum environment. For the *in situ* pressure of 400 mTorr and temperature of 2.5° C we have used, the adsorbed water layer is found to be about 10 Å thick by analyzing relative core peak intensities using the SESSA program [43]. Figure 9(b) shows a typical O 1*s* spectrum, with four distinct chemical components clearly resolvable, including water in the gas phase above the sample. In Figure 9(c), it is remarkable that all four oxygen components show the effects of the SW scanning through the surface, including even the gas-phase water, and that they each have distinct RC shapes. Figure 9(d) now compares the rocking curves for Cs 4*d* and Na 2*p* intensities, and we find a small but reliable shift of 0.04° in the steeply sloping regions of the two curves near the Bragg angle of the multilayer, and also a different shape in the wings away from these regions, with the Cs *4d* RC having higher intensity both below and above the Bragg angle. These differences immediately indicate that the two ions have a different depth distribution. Fully analyzing the rocking curves from all of the resolvable chemical species using a specially-written program [8] leads to the excellent fits of theory to experiment shown in Figure 9(e) and the depth distributions shown in Figure 9(f).

A subsequent SWAPPS study has made use of hard x-ray excitation to look through a thin film of electrolyte from an operating electrochemical cell in which Ni was being oxidized in a KOH solution [44], using what has been termed variously the "meniscus" or "dip-and-pull" or "dipstick" method [45]. In this approach, an active electrode is pulled from a working cell, leaving a thin layer of electrolyte on the surface that is in equilibrium with that in the cell, thus permitting photoemission and SWAPPS measurement in *operando*.

These results thus point to the use of such SWAPPS measurements, particularly with hard x-ray excitation to probe thicker electrolyte layers and/or to penetrate thin-film windows enclosing the cell, for studying the interface region of surface reactions in a much more precise element- and chemical state- resolved way than has previously been possible, with a broad range of applications including catalysis, energy- and environmental- research.

2.6 Near-total reflection measurement of the charge accumulation at the interface between a ferroelectric and a doped Mott insulator: $BiFeO_3/(Ca_{1-x}Cex)MnO_3$

We have already mentioned that going into the total reflection regime has for some time been utilized to enhance surface sensitivity and reduce inelastic backgrounds in XPS [13,14,15,16,17]. Additional interference effects with reflection at buried interfaces can provide useful structural information on going into total reflection, with this method possessing the advantage that it can be applied to any material, but in particular, bilayer or trilayer samples that are simpler to grow than multilayers.

We illustrate the NTR approach in Figure 10 with some HXPS experimental data and x-ray optical simulations for a bilayer sample of ferroelectric $BiFeO_3$ on top of a Ce-doped Mott insulator $(Ca_{0.96}Ce_{0.04})MnO_3$ (BFO on CCMO), a system recently studied as leading to strong ferroelectric control of the Mott insulator-metal transition in the two-dimensional electron gas at the interface between them [46]. The photon energy was 2.8 keV, thus permitting the study of a buried interface in a sample of 10 nm BFO on 210 nm of CCMO, grown on a $YAlO_3$ substrate, as shown in Figure 10(c). The intensities of various core level peaks have been monitored as a function of incidence angle : C 1*s* from the surface contaminant overlayer, Bi 4*f* from BFO, and two components of Ca 2*p* from CCMO that are clearly resolved in the spectra of Figure 10(a), which were obtained at angles for which the calculations of electric field intensity in Figure 10(b) for the final optimized sample geometry in Figure 10(c) indicate enhanced sensitivity to the BFO/CCMO interface (higher binding energy) or the bulk of the CCMO (lower binding energy). The angular dependent raw data for these four intensities are shown in Figure 10(d), and they clearly exhibit differences in both the final decrease to zero at total reflection and the oscillatory standing-wave interference phases seen for higher angles. The comparison of theory for the optimized sample geometry and experiment in Figure 10(e) further shows excellent agreement, and the thickness of the ~1 nm charge accumulation region in the CCMO derived by fitting the NTR experimental results for the two Ca components to theory agrees well with a separate analysis of small shifts in STEM-EELS Mn L_3 near-edge features, again confirming the utility of NTR photoemission in such studies.

The oscillations in Figures 10(d) and 10(e) are due to reflections and interference at the surface and the two buried interfaces in the sample, and the peaks in intensity near 0.9° to the spreading of the x-ray beam along the spectrometer entrance slit direction and the concentration of electric field near the surface, the latter an effect first observed and explained by Henke [13]. Important additional features are the differences in phase of the oscillations for Bi and Ca shown in Figure 10(d), which are useful through the process of optimizing the sample geometry to fit experiment in deriving depth-dependent interface information.

As general background, it is also worth noting that SW effects in hard x-ray reflection and emission of the type shown in Figure 8 have been used previously, e.g. to study the distribution of ionic species in solution above oxide surfaces [12,47], but with our photoemission approach having the advantage of chemical-

and spin- state specificity through core level shifts and fine structure, as well as the ability to look directly at VB DOS changes at interfaces.

2.7 Atomic-plane Bragg reflection standing-wave hard x-ray ARPES: element- and momentum- resolved electronic structure of GaAs and the dilute magnetic semiconductor $Ga_{1-x}Mn_xAs$

As an introduction to this topic, we will briefly discuss the first application of HARPES to the elucidation of the electronic structure of a material over which some controversy existed: the prototypical dilute magnetic semiconductor (DMS) $Ga_{1-x}Mn_xAs$, with $x \approx 0.03$-0.06. The key question here was the nature of the Mn-induced states, and whether they represent a narrow impurity band that is separated cleanly from the GaAs *p* valence bands, or whether these states are merged with the GaAs impurity bands. In the former case, the so-called double-exchange mechanism would be active in producing ferromagnetism and in the latter, it would be what has been referred to as *p-d* exchange. Gray et al. [48] have studied a sample with composition $Ga_{0.97}Mn_{0.03}As$, with 3.2 keV photon energy. Beyond a light acid etch in air to remove surface oxide, no other surface preparation was done, illustrating a key advantage of more bulk sensitive HARPES. In Figure 11, the HARPES data from GaAs and $Ga_{0.97}Mn_{0.03}As$ are compared with theory, with very accurate one-step photoemission calculations shown in (a) and (b), experimental results in (c) and (d), and the angle-resolved intensity from a core-like, predominantly As 4*s*, band at about 12 eV binding energy that exhibits hard x-ray photoelectron diffraction (HXPD) effects in (e) and (f), respectively. The intensity distributions of the $Ga_{0.97}Mn_{0.03}As$ are in all panels smeared out relative to those in GaAs, as might be expected from the presence of the Mn atoms which disturb the long-range periodicity. One-step theory is in agreement with experiment in predicting these differences, with other theoretical results and analysis being presented elsewhere [48]. Further analysis of the ***k***-resolved results, including angle-averaged differences between GaAs and $Ga_{0.97}Mn_{0.03}As$, with special attention to the region very near E_F permitted concluding that we must for this material consider both *p-d* exchange and double exchange to explain its ferromagnetism. This conclusion has also been essentially confirmed by soft x-ray resonant ARPES [49].

It is also interesting to note in these data the shift in the symmetry center of the ARPES results compared to the symmetry center of the HXPD pattern of the As 4*s* band; this is due to the photon momentum, a non-dipole effect that must be included in the conservation of ***k***, as discussed above and by Gray et al. [22].

This study thus represents a first application of HARPES to a complex system whose electronic structure was in debate, and it suggests a wide area of application in the future for studying the bulk electronic structure of complex materials. The future prospects and limitations for HARPES have been discussed in more detail elsewhere [1,22].

Beyond this, we now discuss standing-wave HARPES (SW-HARPES) making use of Bragg reflection from atomic planes, so as to assess the possibility of using this technique to derive element- and momentum- resolved electronic structure, possibly also as a function of spatial position within the unit cell. Going to energies above about 2 keV for which the x-ray wavelength is less than 6 Å permits creating standing-waves due to reflection from crystal planes separated by greater than 3 Å, with the SW then scanning by half a cycle through the unit cell and along the [$hk\ell$] direction as photon energy is moved over the appropriate Bragg condition.

We have noted that several prior studies have used Bragg reflection from atomic planes to create standing waves that are then scanned through the unit cell via photon energy scans, with combined core- and valence- data then being used to deconvolute densities of states into their element-specific contributions [34,35,50]. These prior measurements have all been carried out in the Brillouin-zone-averaged MEWDOS or XPS limit. However, with cryogenic cooling, such experiments should also be possible in an angle-resolved mode, in which case the HARPES results could represent element- and momentum- resolved sampling at different points in the Brillouin zone, a truly unique type of measurement.

Although soft x-ray resonant photoemission can provide somewhat similar information on element- and ***k***-resolved electronic structure [49], the spatial phase information provided by the SW, coupled with core level intensities, should permit a much more quantitative decomposition of the VB intensities into their atomic components and spatial distribution that is furthermore more truly bulk sensitive.

We now discuss some encouraging proof-of-principle results of this kind for the same two systems of GaAs(001) and the dilute magnetic semiconductor (Ga,Mn)As(001), using an HXPS facility particularly suited for this at Diamond Light Source Beamline I09 [51]. Some of these results are summarized in Figure 12. In Figure 12(a), we illustrate one of two experimental geometries used: (111) reflection, with the SW then scanned along the [111] direction, and four possible positions of its antinodes indicated. In Figure 12(b), the energy scans of As 3*d* and Ga 3*d* are shown, and they are clearly very different, due to their different positions in the unit cell along the [111] direction; these results also agree well with prior core-level data of this type for GaAs(111) by Woicik et al. [35]. In Figure 12(c), analogous scans for a sample consisting of ~100 nm of $Ga_{0.95}$ $Mn_{0.05}As$ deposited on a GaAs(001) substrate, are shown. Two different Bragg reflections are seen here, a narrower structure from the substrate and a wider structure for the finite-thickness $Ga_{0.95}$ $Mn_{0.05}As$, with differences between the Ga and As curves associated with both of them. Figure 12(d) shows similar data for the same sample, but with (311) reflection, and with the addition of an energy scan for Mn 2*p*; although noisy due to the low concentration of Mn, it is clear that the Mn curve agrees with that for Ga, indicating a substitutional position of the Mn atoms

In Figure 13, we consider adding elemental sensitivity to HARPES via such SW measurements. In Figure 13(a) we show HARPES results for GaAs and $Ga_{0.95}$ $Mn_{0.05}As$, over a wider angular range than the data in Figure 11, for a photon energy of 2719 eV in the middle of the energy scan. Overlaid on these data are light blue curves calculated for direct transitions from the ground-state electronic structure of both materials, with CPA again being used for the doped material, to a strictly free-electron final state (FEFS), a very useful method of initial analysis of HARPES data [22,48] that permits determining the exact orientation of the sample. This method is accurate to less than 0.5°, including a small tilt of the sample for the present case and a slight difference in geometry for the two samples. In Figure 13(b), we show the experimental data again, but after a procedure making use of the core-level energy scans for Ga 3*d* and As 3*d* that permits identifying the element-resolved contributions to each pixel. This method proceeds in the following way. We first assume that the intensity in each HARPES pixel can be described as a superposition of a contribution from As and from Ga(or Mn) as:

$$I_{HARPES}(E_B,\vec{k},h\nu) \approx I_{As}(E_B,\vec{k},h\nu) + I_{Ga(Mn)}(E_B,\vec{k},h\nu) \quad [3]$$

Then, the energy-dependence of each pixel is projected into fractional As and Ga(Mn) components by using a least-squares comparison to the core-level intensities as:

$$I_{Proj}(E_B,\vec{k},\mathrm{h}\nu) = f_{As}(E_B,\vec{k})I_{As3d}(h\nu) + f_{Ga(Mn)}(E_B,\vec{k})I_{Ga3d(Mn2p)}(h\nu), \quad [4]$$

where $f_{Ga(Mn)} = 1 - f_{As}$. An important point in using this method for analyzing such results is that it has long been realized through various theoretical studies that the matrix elements and cross sections for valence photoemission are increasingly controlled by the inner spatial regions of each atom involved [52,53,54], thus making the use of core-level intensities on the same atom at nearly the same kinetic energy a good approximation for such SW projection procedures. This sort of projection has been used previously to analyze SW MEWDOS spectra [34,35,50], but not with ***k*** resolution. Once the two *f* quantities have been determined, they are applied to each pixel, and a color scale going from +1.0 = maximum Ga(Mn)/minimum As to -1 = maximum As/minimum Ga(Mn) is applied to the data. The result is the plot shown in Figure 13(b), which reveals a dramatic difference between the top and bottom sets of bands, which are strongly As and the middle bands, which are strongly Ga(Mn). For the doped sample, one

can even see evidence of what is probably weak Mn intensity in the upper bands over 0-6 eV, consistent with prior conclusions that Mn affects the entire band structure [48, 49]. So we now have an element- and ***k***-resolved band structure, directly derived from experiment.

Theoretical calculations also support this method, as shown in Figure 13(c). Here, we show element-resolved Bloch spectral functions, computed for the same trajectory in ***k***-space as derived from the FEFS calculations in Figure 13(a), with CPA used for the doped material, and in the same color scale. There is excellent qualitative agreement as to the major elemental ingredients in each band. We do not expect fully quantitative agreement, as matrix elements are not included in the theoretical calculations, but future progress with one-step theory should permit going to this limit as well.

We thus view these results as most positive for the future use of SW-HARPES to study the element- and momentum- resolved bulk electronic structure of many multicomponent materials. Making use of simultaneous analysis of multiple Bragg reflections, as in prior MEWDOS-level studies [50], will improve the accuracy of localizing the electronic structure, both in momentum and within the unit cell.

3 Conclusions and future outlook

In conclusion, the use of higher-energy excitation in photoemission, either in the soft x-ray (from a few hundred to ca. 2 keV) or hard x-ray (from 2 keV and up to ca. 10 keV) permits looking at buried interfaces and/or bulk electronic structure that are not accessible with the lower-energies of traditional ARPES. Adding standing-wave excitation through either x-ray reflection from a multilayer heterostructure or atomic planes, enhances the depth resolution of the measurement significantly. Tuning the photon energy to various positions near strong absorption resonances can significantly increase the standing-wave modulation and also permits tuning its phase and thus anti-node position.

Through the example studies presented here, we believe it is clear that such techniques should permit studying a very wide variety of oxide and other interfaces in the future, including even the liquid-solid interface. As more intense and more highly focused radiation sources become available, the precision of such measurements will be enhanced, including the ability to add lateral resolution through simultaneous photoelectron microscopy in one of its several modalities. Adding time resolution through free-electron laser or high-harmonic generation sources will also be an exciting new direction. Varying polarization will also permit studying magnetic systems with higher precision, as for example, the depth variation of in-plane and perpendicular-to-plane magnetization at interfaces. Simultaneous spin detection will permit doing what one might call the complete photoemission experiment, providing resolution in energy, momentum, and spin, in three spatial dimensions through the interface, or through the unit cell, and in time.

Acknowledgements

The specific sources of funding for the various studies presented here are listed in the publications cited. Beyond this, C.S.F. has also been supported during the writing of this chapter for salary by the Director, Office of Science, Office of Basic Energy Sciences (BSE), Materials Sciences and Engineering (MSE) Division, of the U.S. Department of Energy under Contract No. DE-AC02-05CH11231, through the Laboratory Directed Research and Development Program of Lawrence Berkeley National Laboratory, and through a DOE BES MSE grant at the University of California Davis from the X-Ray Scattering Program under Contract DE-SC0014697. A.X.G acknowledges support during the writing of this chapter from the U.S. Army Research Office, under Grant No. W911NF-15-1-0181.

Figure captions and figures

Figure 1: Schematic illustration of the formation of a standing wave in first-order Bragg reflection from a multilayer mirror, together with the equations describing the standing wave period λ_{SW}. The standing wave can be scanned through the sample, which might be the mirror, or grown on top of the mirror, in the three ways indicated: a rocking curve, a photon energy scan, or a wedge scan. The equations describe the overall intensity for a given photon energy $h\nu$, reflectivity R, incidence angle θ_{inc}, phase shift on reflection of φ, position z of an atom of interest, and the fraction of atoms in coherent positions supporting the Bragg reflection.

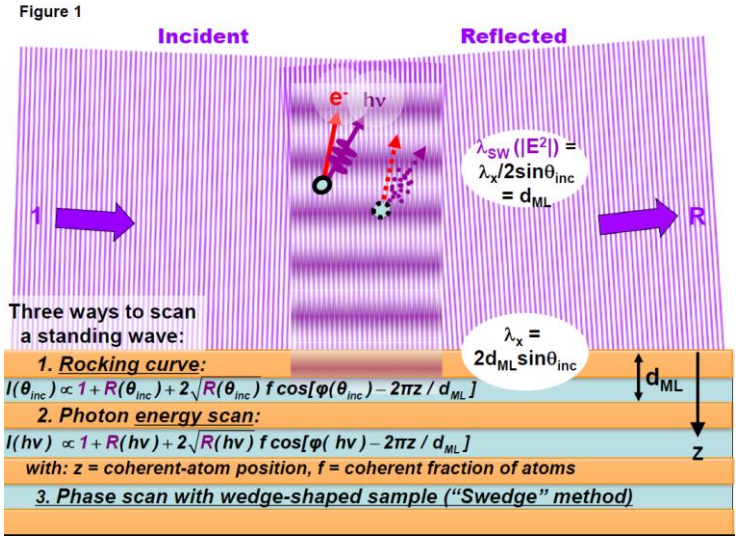

Figure 2: (a) The sample and experimental configuration for a standing-wave XPS and ARPES study of a $La_{0.67}Sr_{0.33}MnO_3/SrTiO_3$ (LSMO/STO) multilayer sample, with dimensions indicated, together with expressions describing both first-order Bragg reflection and Kiessig fringes. (b) The absorption coefficient, (expressed as β, the imaging part of the index of refraction), of this multilayer for photon energies scanning through the La $3d_{5/2}$ = La M_5 absorption resonance. (c) The reflectivity on scanning angle through the Bragg reflection as a function of photon energies going over the resonance. From these data, 833.2 eV was chosen to maximize reflectivity and thus SW modulation. Experimental data from the Advanced Light Source (ALS). [From ref. 10].

Figure 2

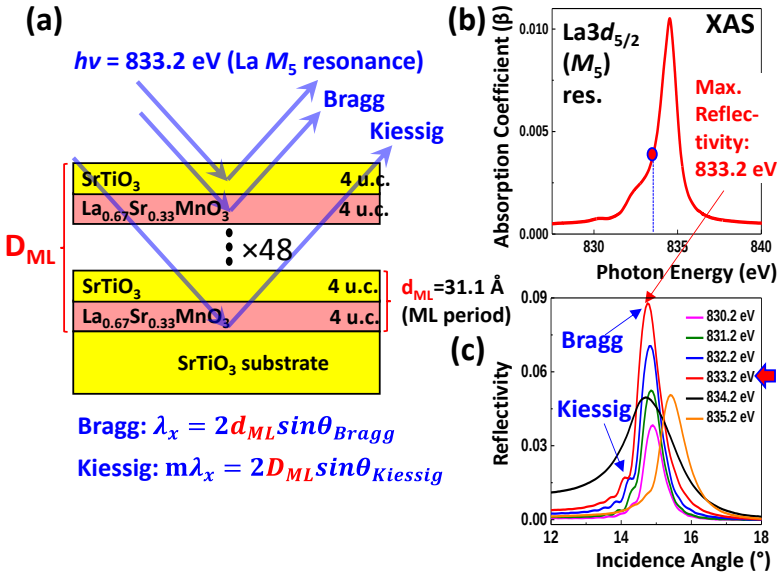
(a)
hν = 833.2 eV (La M5 resonance)
Bragg
Kiessig
SrTiO3 4 u.c.
La0.67Sr0.33MnO3 4 u.c.
×48
SrTiO3 substrate
DML
dML=31.1 Å
(ML period)
Bragg: λx = 2dML sinθBragg
Kiessig: mλx = 2DML sinθKiessig
(b)
La3d5/2
(M5)
res.
XAS
Max.
Reflec-
tivity:
833.2 eV
Absorption Coefficient (β)
Photon Energy (eV)
(c)
Bragg
Kiessig
830.2 eV
831.2 eV
832.2 eV
833.2 eV
834.2 eV
835.2 eV
Reflectivity
Incidence Angle (°)

Figure 3: X-ray optical calculations using the program of ref. 8 of the effect of tuning photon energy to a position below and above the Gd M_5 absorption resonance on the location of the standing wave, for a 20-bilayer multilayer of $SrTiO_3$ and $GdTiO_3$ with bilayer thickness of 35.5 Å. (a) The variation of the real (δ) and imaginary (β) parts of the index of refraction over the Gd M_5 absorption resonance, from experimental x-ray absorption data and Kramers-Kronig analysis. (b), (c) The depth distribution of the standing-wave electric field intensity as the incidence angle is scanned through the 1st-order Bragg reflection of the multilayer, for the two photon energies 1181 eV and 1187 eV. Note the vertical shift in the antinode position of the SW, from sensitivity to the STO surface at 1181 eV to sensitivity to the GTO/STO interface at 1187 eV. Kiessig fringes are also evident in these calculations as the nearly vertical ripples in the field intensity.

Figure 3

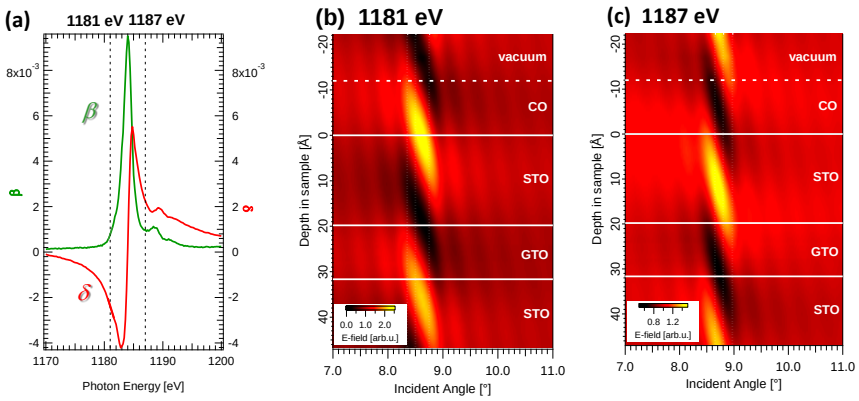

Figure 4: Calculated parameters for estimating the feasibility of ARPES at higher energies including (a) contours for various photon energies to yield a photoemission Debye-Waller factor W(T) of 0.5 at a typical LHe cryocooling temperature of 20K, and (b) the recoil energy for all atoms as a function of photon energy. Values for two first demonstration cases W and GaAs studied with hard X-rays [22] are highlighted. [From ref. 19]

Figure 4

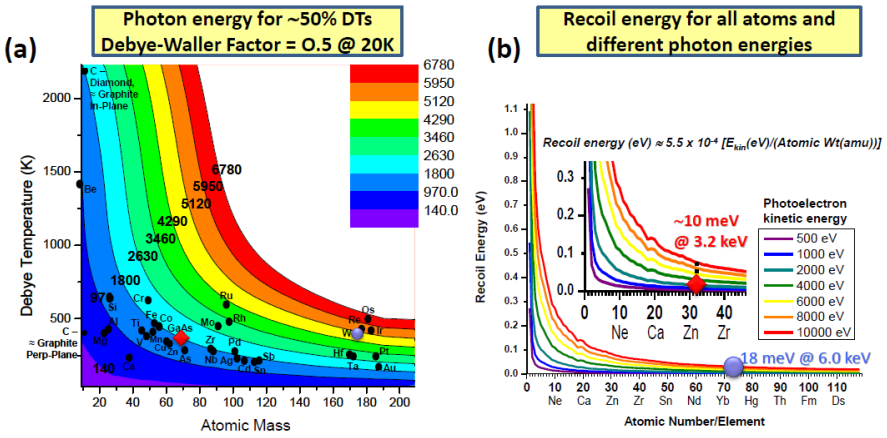

Figure 5: (a) Results of an x-ray optical analysis of both soft- and hard- x-ray rocking curves of core-level intensities from all elements in the multilayer LSMO/STO sample of Figure 2(a), with the final best-fit to theory being for a multilayer period d_{ML} that changes about 6% with depth as shown in (b), and with interface concentration/roughness profiles as in (c). The results in (b) and (c) have also recently been quantitatively confirmed by TEM/EELS. Experimental data from the ALS and SPring-8. [From refs. 10 and 36].

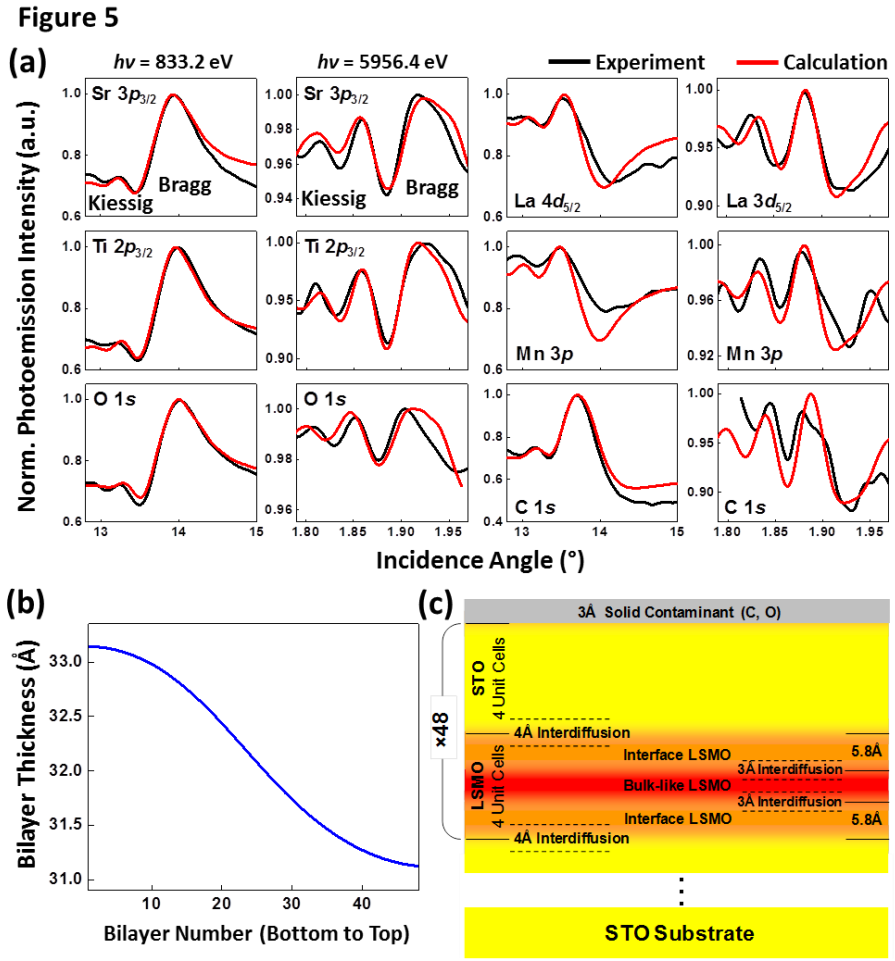

Figure 6: Standing-wave rocking-curve spectroscopy with an 833 eV excitation energy just below the La M_5 resonance to enhance reflectivity from the 48-bilayer multilayer of $SrTiO_3/La_{0.7}Sr_{0.3}MnO_3$ shown in Fig. 2(a). (a) The evolution of Mn 3*s* and 3*p* and Ti 3*s* core-level binding energies and intensities through a rocking curve. (b),(c) The change in binding energy and multiplet splitting for Mn 3*p* and Mn 3*s*. (d) The variation of the standing-wave field strength through the same angle range as (a). Is is concluded that Mn 3*p* only shows a shift near the LSMO/STO interface. Experimental data from the ALS. [From ref. 10.]

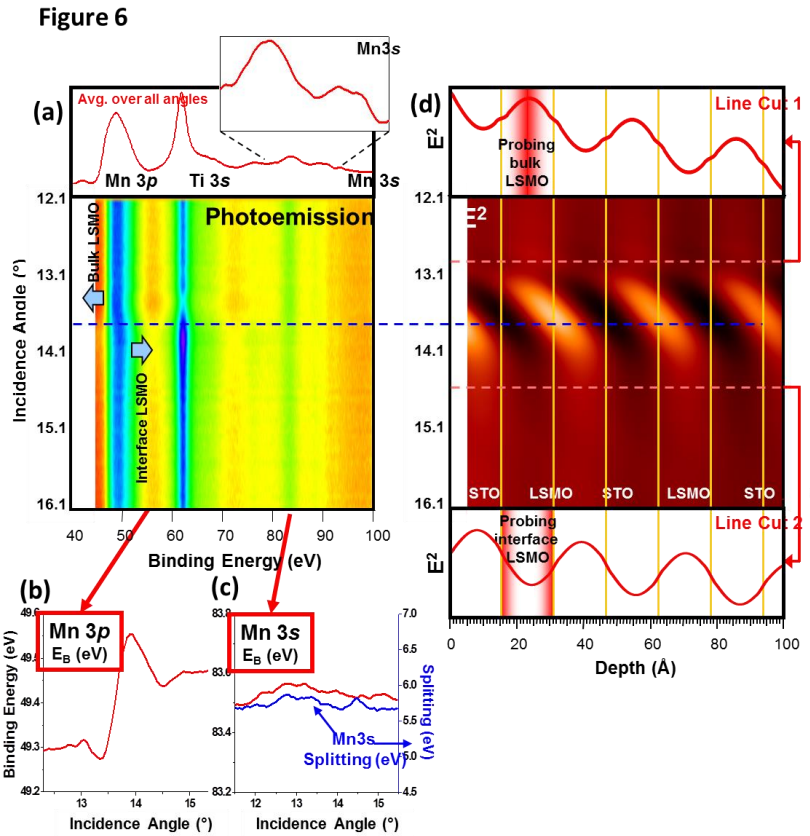

Figure 7: Depth-resolved standing-wave ARPES (SWARPES) measurements from the LSMO/STO superlattice shown in Fig. 2(a), again at 833 eV photon energy. (a) An angle-integrated spectrum spanning a binding-energy window from +1 eV to -9 eV, and including all the major features of the valence-bands, labeled 1 – 5, with their origins and approximate atomic-orbital characters indicated. (b) SWARPES data for these five energies in a bulk-LSMO sensitive SW measurement geometry. Shown are XPD- and-DOS- normalized angle-resolved (k_x,k_y) photoemission intensity maps of the Mn 3d e_g (1), Mn 3d t_{2g} (2) derived states, the largely STO-derived states (3 and 4), and the valence-band bottom states (5) which were finally assigned to LSMO. (c) As (b), but for an LSMO/STO-interface sensitive measurement geometry of the SW. (d) Bulk-minus-interface difference (k_x,k_y) maps based on (b) and (c), revealing the most significant differences for the LSMO-derived Mn 3d e_g and Mn 3d t_{2g} states at the interface between STO and LSMO, and the dispersive valence-band bottom bands 5, probably from LSMO. The intensity scales at right indicate the relative amplitudes of the effects. Experimental data from the ALS. [From ref. 36]

Figure 7

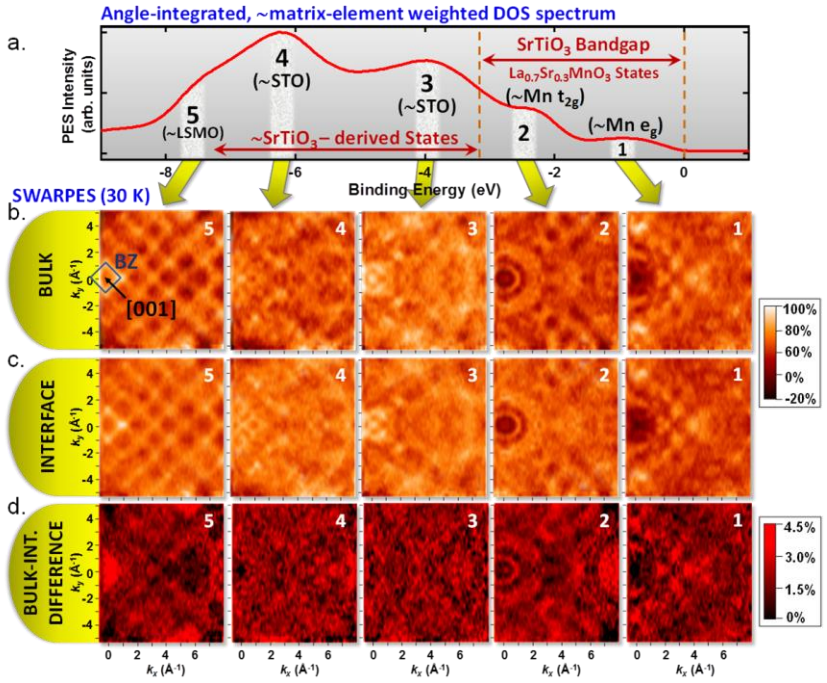

Figure 8: Experimental and theoretical results from a combined standing-wave and resonant photoemission study of a $SrTiO_3/GdTiO_3$ multilayer. (a) The sample configuration. (b) Normal-emission Ti L_2 -resonant ARPES at 465 eV over the 2DEG and LHB features near the Fermi level, as binned in five separate regions A to E. (d) Experimental (right panel) and simulated (left panel) Gd M_5 resonant standing-wave photoemission at 1187 eV, emphasizing the interface (cf. Figure 3(c)), including rocking curves for O 1s, C 1s (surface impurity), Sr 3d, Gd 4f, and valence-level intensity for the 2DEG and the LHB, as derived by peak fitting spectra such as those in Figure 8(b). Simulations are shown for the 2DEG for its being distributed throughout the STO layer (turquoise), and for it occupying only one unit cell near the interface (blue). (e) Binding energy-k_x SW-ARPES image at an interface sensitive Gd M_5-resonant energy of 1187 eV, compared to theoretical calculations for the multilayer using hybrid functionals. Experimental data from ALS and the Swiss Light Source (SLS). [From ref. 11]

Figure 8

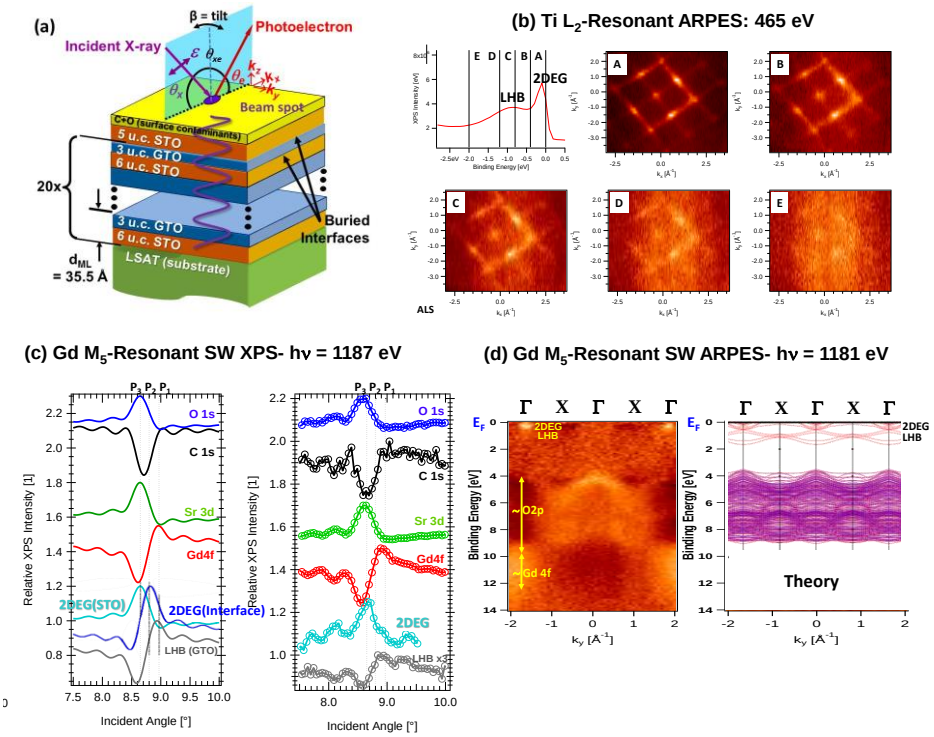

Figure 9: First experimental results for standing-wave ambient pressure photoemission (SWAPPS) from an Fe_2O_3 film grown on a Si/Mo multilayer mirror whose surface was exposed to CsOH, NaOH, and water vapor at 400 mTorr and 2.5° C. The SW is moved through the surface by scanning the incidence angle through the 1st order Bragg condition (cf. Figure 1). (a) The sample configuration. (b) A typical O 1s spectrum, with four distinct chemical species unambiguously identified. (c) The variation of the O 1s intensities of the four species, with all showing strong and distinct variations as the standing wave moves by half of a cycle through the interface. (d) A comparison of the rocking curves of Cs and Na, indicating a shift of ~0.04° near the Bragg angle and different behavior in the wings of the curves. (d) Comparison of experimental and calculated rocking curves for all elements and chemically-resolved peaks, for the final sample structure, as shown in (f). Experimental data are from ALS. [From ref. 40]

Figure 9

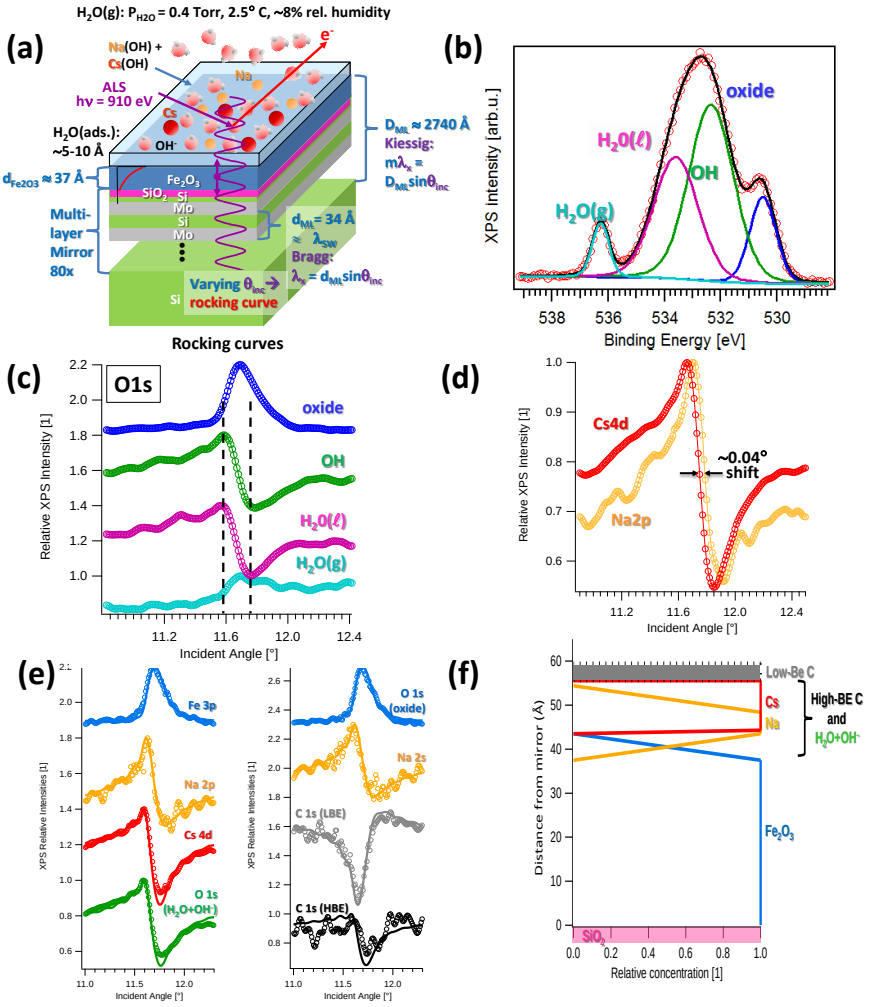

Figure 10: Results of using near total reflection (NTR) HXPS on a single interface in a complex oxide system: a bilayer of $BiFeO_3$ (BFO) and Ce-doped $CaMnO_3$ (CCMO) grown on an $YAlO_3$ substrate. The photon energy is 2.8 keV. (a) The Ca 2p spectra at two incidence angles emphasizing the high-binding-energy (interface) and low-binding-energy (bulk) CCMO regions, respectively. (b) The calculated electric field strength as a function of depth and incidence angle for the sample configuration in (c), as derived by fitting x-ray optical theory to Ca 2p, Bi 2p, and C 1s intensities as a function of angle. (d) The normalized experimental intensity variation of C 1*s*, Bi 4*f*, HBE Ca 2*p* and LBE Ca 2*p* with incidence angle over the NTR region, showing the systematic trend in the approach to total reflection, with peaks deeper within the sample turning off first. (e) The optimized final fits of x-ray optical calculations to the data in (e), for the sample configuration in (b). Experimental data from the ALS. [From Ref. 18]

Figure 10

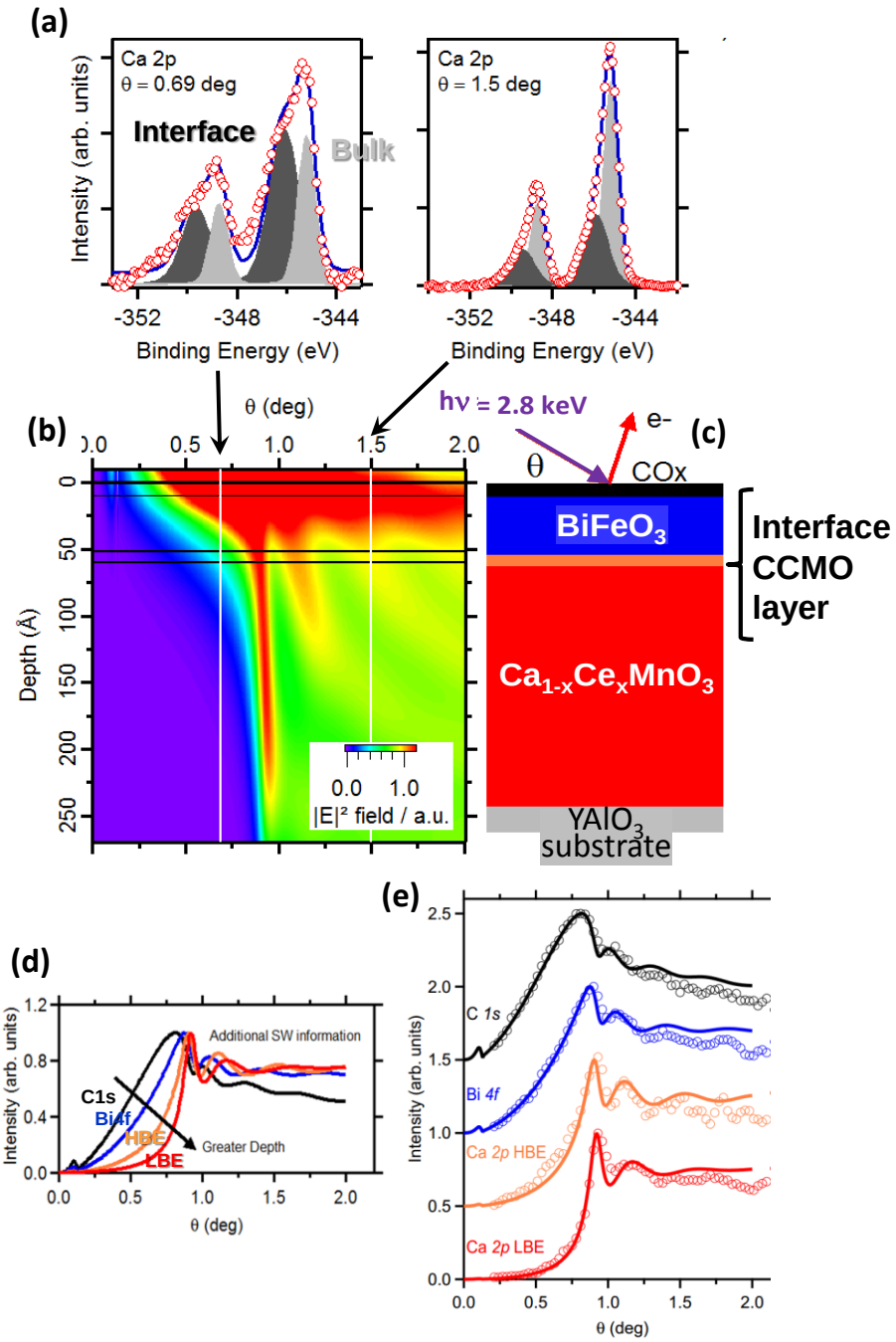

Figure 11: HXPS and HARPES from GaAs and the dilute magnetic semiconductor Mn-doped GaAs. A photon energy of 3.2 keV was used. (a) and (b) show calculated HARPES patterns for the two materials in the same experimental geometries as the experimental results of (c) and (d). (e) and (f) show the same kind of experimental data for the highly localized and nearly purely As 4*s* band, which shows no band dispersions in energy, and exhibits only hard x-ray photoelectron diffraction (HXPD) variations in angle. The dashed lines indicate the slight shift between the center of symmetry of the HXPD, which is linked to the surface normal of the sample, and the center of symmetry in k_x, which is shifted due to the photon momentum. Experimental data from SPring-8. [From Ref. 48]

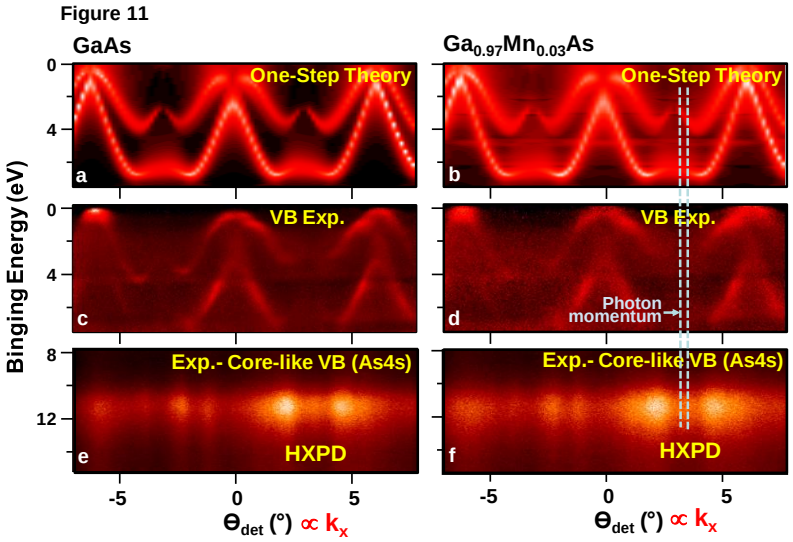

Figure 12: Standing-wave HXPS and HARPES from GaAs(001) and the dilute magnetic semiconductor Mn-doped GaAs (Ga,Mn)As also in (001) surface orientation. Photon energies were 2.7 keV and 3.6 keV. (a) The schematic scanning of the SW along the [111] direction as the photon energy is scanned over the (111) Bragg diffraction condition. (b) The variation of As 3*d* and Ga 3*d* intensities through such an energy scan, with obvious strong differences in behavior. (c) A similar energy scan for a sample with ~100 nm of $Ga_{0.95}Mn_{0.05}As$ grown on GaAs(001). Two Bragg peaks are observed, due to the slight difference in the lattice constant of the (Ga,Mn)As, with similar differences between As 3*d* and Ga 3*d* in going over both. (d) A similar energy scan for (Ga,Mn)As but with (311) diffraction, and Mn 2*p* included. The near identity of the curves for Ga and Mn indicates a high degree of substitutional sites for Mn. Experimental data from Diamond. [From ref. 51]

Figure 12

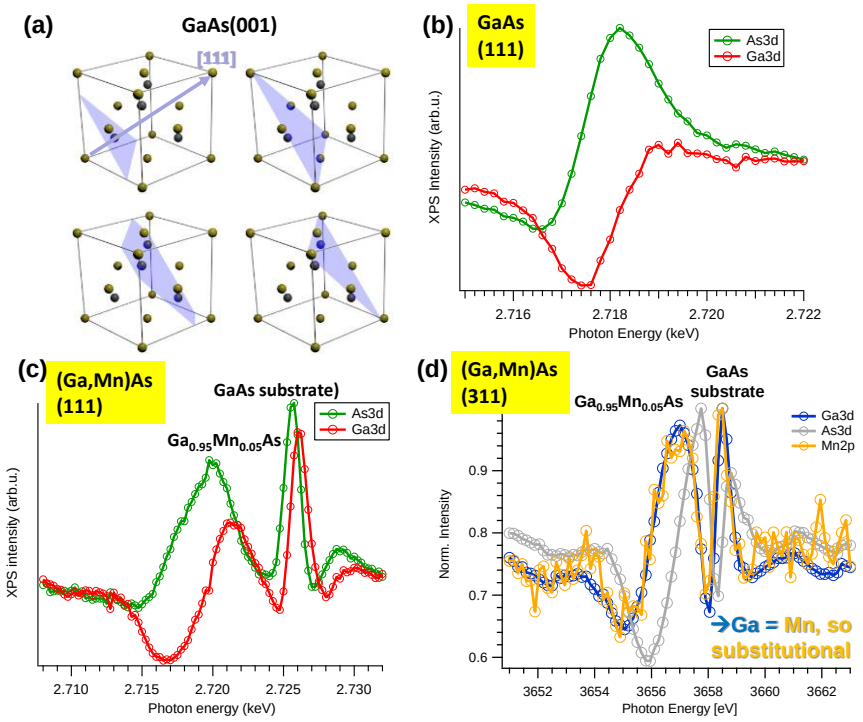

Figure 13: Projection of SW-HARPES data into element-resolved components. (a) Experimental data for GaAs and (Ga,Mn)As in a (111) reflection geometry, with photon energy of ~2.7 keV. The light gray curves are free-electron final-state (FEFF) calculations used to determine the precise sampling in ***k***–space, which was slightly different for the two samples. (b) Experimental decomposition into Ga+Mn and As components using core-level intensities and Equations [3] and [4]. (c) Local-density calculations of element-resolved Bloch spectral functions using the coherent potential approximation (CPA) for (Ga,Mn)As, with the same color scale of maximum Ga,Mn = 1.0 and maximum As = -1.0 as in (b). Experimental data from Diamond. [From ref. 51]

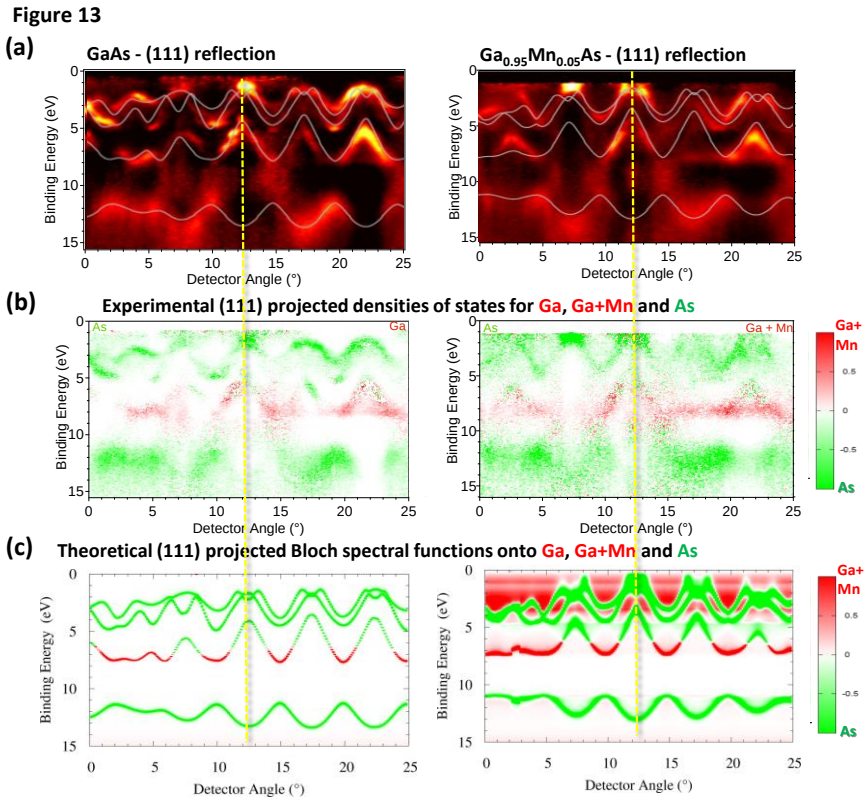

References

1 C. S. Fadley, Synchrotron Radiation News 25, 26 (2012)

2 *Hard X-ray Photoelectron Spectroscopy (HAXPES)*, J. C. Woicik, Editor, Springer Springer Series in Surface Sciences, Volume 59 (2016).

3 *The X-Ray Standing Wave Technique-Principles and Applications*, J. Zegenhagen and A. Kazimirov, Editors (World Scientific Publishing, 2013)

4 C. S. Fadley, J. Electron Spectrosc. 178–179 (2010) 2–32.

5 C. S. Fadley, J. Electron Spectrosc. 190, 165-179 (2013), special issue dedicated to hard x-ray photoemission, W. Drube, Editor.

6 A. X. Gray, J. Electron Spectrosc. 195, 399 (2014).

7 C. S. Fadley and S. Nemšák, in special issue of the Journal of Electron Spectroscopy dedicated to Structure Determination and Wave-Function Analysis, H. Daimon, A. Hishikawa, and C. Miron, Editors, J. Electron Spectrosc. 195, 409–422 (2014).

8 S.-H. Yang, A. X. Gray, A. M. Kaiser, B. S. Mun, J. B. Kortright, and C. S. Fadley, J. Appl. Phys. 113, 073513 (2013)

9 S.-H. Yang, B.S. Mun, N. Mannella, S.-K. Kim, J.B. Kortright, J. Underwood, F. Salmassi, E. Arenholz, A. Young, Z. Hussain, M.A. Van Hove, and C.S. Fadley, J. Phys. Cond. Matt. 14, L406 (2002))

10 A. X. Gray, C. Papp, B. Balke, S.-H. Yang, M. Huijben, E. Rotenberg, A. Bostwick, S. Ueda, Y. Yamashita, K. Kobayashi, E. M. Gullikson, J. B. Kortright, F. M. F. de Groot, G. Rijnders, D. H. A. Blank, R. Ramesh, and C. S. Fadley, Phys. Rev. B 82, 205116 (2010).
11 S. Nemšák, G. Pálsson , A. X. Gray, D. Eiteneer, A.M. Kaiser, G. Conti, A.Y. Saw, A. Perona, A. Rattanachata, C. Conlon, A. Bostwick, V. Strocov, M. Kobayashi, W.Stolte, A. Gloskovskii, W. Drube , M.-C. Asencio, J. Avila, J. Son, P. Moetakef, C. Jackson, A. Janotti, C. G. Van de Walle , J. Minar, J. Braun, H. Ebert, J.B. Kortright, S. Stemmer, and C. S. Fadley, Phys. Rev. B 93, 245103 (2016)
12 M. J. Bedzyk ,G. Materlik, M. V. Kovalchukas, Phys. Rev. B 30, 2453 (1984)
13 B. L. Henke, Phys. Rev. 6, 94 (1972).
14 M. Mehta and C.S. Fadley, Chem. Phys. Lett. 46, 225 (1977).
15 M. J. Chester, T. Jach, and S. Thurgate, J. Vac. Sci. Technol. B11, 1609 (1993); M. J. Chester and Terrence Jach, Phys. Rev. B 48, 17262 (1993).
16 J. Kawai, S. Hayakawa, Y. Kitajima, Y. Gohshi, Adv. X-Ray Chem. Anal. Jpn. 26s 97(1995).
17 J. Kawai, review in J. Electron Spectrosc. 178–179, 268–272 (2010).
18 M. Marinova, J. E. Rault, A. Gloter, S. Nemšák, G. K. Pálsson, J.-P. Rueff, C. S. Fadley, C. Carrétéro, H. Yamadag, K. March, V. Garcia, S. Fusil, A. Barthélémy, O. Stéphan, C. Colliex, M. Bibes, Nano Lett. 15, 2533−2541 (2015).
19 C. Papp, L. Plucinski, J. Minar, J. Braun, H. Ebert, and C. S. Fadley, Phys. Rev. B 84, 045433 (2011).
20 M. Sagurton, E. L. Bullock, and C. S. Fadley, Surf. Sci. 182, 287 (1987)
21 J. Braun, J. Minar, S. Mankovsky, L. Plucinski, V. N. Strocov, N. B. Brookes, C. M. Schneider, C. S. Fadley, H. Ebert, Phys. Rev. B 88, 205409 (2013).
22 A. X. Gray, C. Papp, S. Ueda, B. Balke, Y. Yamashita, L. Plucinski, J. Minár, J. Braun, E. R. Ylvisaker, C. M. Schneider, W. E. Pickett, H. Ebert, K. Kobayashi and C. S. Fadley, Nat. Mat. 10, 759 (2011).
23 M. J. Bedzyk, D. Bilderback, J. White, H. D. Abrufia, and M. G. Bommarito, J. Phys. Chem. 90, 4926 (1986).
24 J. B. Kortright and A. Fischer-Colbrie, J. Appl. Phys. 61, 1130 (1987).
25 S.-K. Kim and J. B. Kortright, Phys. Rev. Lett. 86, 1347 (2001)
26 S.-H. Yang, B. S. Mun, A. W. Kay, S.-K. Kim, J. B. Kortright, J.H. Underwood, Z. Hussain, and C.S. Fadley, Surf. Sci. Lett. 461, L557 (2000).
27 S.-H. Yang, B. S. Mun, N. Mannella, A. Nambu, B.C. Sell, S. B. Ritchey, F. Salmassi, S. S. P. Parkin, C. S. Fadley, J. Phys. C Solid State 18, L259–L267 (2006).
28 A. X. Gray, F. Kronast, C. Papp, S.-H. Yang, S. Cramm, I. P. Krug, F. Salmassi, E. M. Gullikson, D.L. Hilken, E. H. Anderson, P. J. Fischer, H. A. Dürr, C. M. Schneider, and C. S. Fadley, Appl. Phys. Lett. 97, 062503 (2010).
29 S.-H. Yang, B. Balke, C. Papp, S. Döring, U. Berges, L. Plucinski, C. Westphal, C.M. Schneider, S. S. P. Parkin, and C. S. Fadley, Phys. Rev. B 84, 184410 (2011).
30 A. A. Greer, A. X. Gray, S. Kanai, A. M. Kaiser, S. Ueda, Y. Yamashita, C. Bordel, G. Palsson, N. Maejima, S.-H. Yang, G. Conti, K. Kobayashi, S. Ikeda, F. Matsukura, H. Ohno, C. M. Schneider, J. B. Kortright, F. Hellman, and C. S. Fadley, Appl. Phys. Lett. 101, 202402 (2012)
31 B.W. Batterman, Phys. Rev. 133, A759 (1964).
32 P. I. Cowan, J. A. Golovchenko, and M. F. Robbins, Phys. Rev. Lett. 44, 1680 (1980).
33 W. Drube, A. Lessmann, and G. Materlik, Rev. Sci. Instrum. 63, 1138 (1992)
34 J. C. Woicik, E. J. Nelson, P. Pianetta, Phys. Rev. Lett. 84, 773 (2000).
35 J. C. Woicik, E. J. Nelson, D. Heskett, J. Warner, L. E. Berman, B. A. Karlin, I. A. Vartanyants, M. Z. Hasan, T. Kendelewicz, Z. X. Shen, and P. Pianetta, Phys. Rev. B 64, 125115 (2001).

36 A. X. Gray, J. Minár, L. Plucinski, M. Huijben, A. Bostwick, E. Rotenberg, S.-H. Yang, J. Braun, A. Winkelmann, D. Eiteneer, A. Rattanachata, A. Greer, G. Rijnders, D. H. A. Blank, D. Doennig, R. Pentcheva, J.B. Kortright, C. M. Schneider, H. Ebert, and C. S. Fadley, Europhys. Lett. 104, 17004 (2013).

37 P. Moetakef, J.Y. Zhang, A. Kozhanov, B. Jalan, R. Seshadri, S.J. Allen, S. Stemmer, Applied Physics Letters **98**, 112110 (2011); P. Moetakef , T.A. Cain, D.G. Ouellette, J.Y. Zhang, D. O. Klenov, A. Janotti, C.G. Van de Walle, S. Rajan, S.J. Allen, S. Stemmer, Applied Physics Letters **99**, 232116 (2011); C. Jackson, P. Moetakef, S.J. Allen, S. Stemmer, Applied Physics Letters **100**, 232106 (2012); P. Moetakef, J.R. Williams, D. G. Ouellette, A. P. Kajdos, D. Goldhaber-Gordon, S.J. Allen, S. Stemmer, Phys. Rev. X **2**, 021014 (2012).

38 W. Meevasana, P. D. C. King, R. H. He, S-K. Mo, M. Hashimoto, A. Tamai, P. Songsiriritthigul, F. Baumberger and Z-X. Shen, Nat. Mat. **10**, 114 (2011).

39 A. F. Santander-Syro, O.Copie, T. Kondo, F. Fortuna, S. Pailhès, R. Weht, X.G. Qiu, F. Bertran, A. Nicolaou, A. Taleb-Ibrahimi, P. Le Fèvre, G. Herranz, M. Bibes, N. Reyren, Y. Apertet, P. Lecoeur, A. Barthélémy, M.J. Rozenberg, Nature 469, 189 (2011) Jan 13;469(7329).

40 S. Nemšák, A. Shavorskiy, O. Karslioglu, I. Zegkinoglou, A. Rattanachata, C.S. Conlon, A. Keqi, P.K. Greene, K. Liu, F. Salmassi, E.M. Gullikson, H. Bluhm, and C.S. Fadley, Nat. Comm. 5, 5441 (2014).

41 *Electrochemical Aspects of Ionic Liquids*, H. Ohno (John Wiley & Sons, 2011).

42 *Mineral-Aqueous Solution Interfaces and Their Impact on the Environment*, G. E. Brown and G. Calas, Geochemical Perspectives **1**, 483-742, with special discussion of the mineral-electrolyte double layer over pp. 552-557.

43 W. Smekal, W. S. M. Werner and C. J. Powell, Surf. Interface Anal. **3**, 1059 (2005); W. S.M. Werner, W. Smekal, T. Hisch, J. Himmelsbach, C. J. Powell, J. Electron Spectrosc. **190**, 137 (2013).

44 O. Karslıoğlu, S. Nemšák, I. Zegkinoglou, A. Shavorskiy, M. Hartl, F. Salmassi, E.M. Gullikson, M.L. Ng, Ch. Rameshan, B. Rude, D. Bianculli, A.A. Cordones-Hahn, S. Axnanda, E.J. Crumlin, P.N. Ross, C.M. Schneider, Z. Hussain, Z. Liu, C.S. Fadley, H. Bluhm, Faraday Soc. Disc. 2015, 180, 35 (2015).

45 S. Axnanda, E.J. Crumlin, B. Mao, S. Rani, R. Chang, P.G. Karlsson, M.O.M. Edwards, M. Lundqvist, R. Moberg, P.N. Ross, Z. Hussain & Z. Liu, Sci. Rep. 5, 09788 (2015).

46 H. Yamada, M. Marinova, P. Altuntas, A. Crassous, L. Bégon-Lours, S. Fusil, E. Jacquet, V. Garcia, K. Bouzehouane, A. Gloter, J. E. Villegas, A. Barthélémy, and M. Bibes, Sci. Rep. 3, 2834 (2013).

47 M.J. Bedzyk, in Surface X-ray and Neutron Scattering. (Vol. 61 of Springer Proceedings in Physics). (eds H. Zabel H. and I.K. Robinson I) Vol. 51,113–117 (Springer-Verlag, 1992) and references therein.

48 A. X. Gray, J. Minar, S. Ueda, P. R. Stone, Y. Yamashita, J. Fujii, J. Braun, L. Plucinski, C. M. Schneider, G. Panaccione, H. Ebert, O. D. Dubon, K. Kobayashi, and C. S. Fadley, Nat. Mat. **11**, 957 (2012).

49 M. Kobayashi, I. Muneta, Y. Takeda, Y. Harada, A. Fujimori, J. Krempasky, T. Schmitt, S. Ohya, M. Tanaka, M. Oshima, and V.N. Strocov, Phys. Rev. B 89, 205204 (2014).

50 S.Thiess, T.- L. Lee, F. Bottin, J. Zegenhagen, Solid State Commun. 150, 553 (2010).

51 S. Nemšák, S. Döring, C. Schlueter, M. Eschbach, M. Gehlmann, L. Plucinski, S. Borek, J. Minar, J. Braun, H. Ebert, T.-L. Lee, C.M. Schneider, C.S. Fadley, unpublished results.

52 U. Gelius and K. Siegbahn, Discuss. Faraday Soc., 54, 257 (1972).

53 C. S. Fadley, in *Electron Spectroscopy: Theory, Techniques, and Applications*, C. R. Brundle and A. D. Baker, Eds. (Academic Press, London, 1978) Vol. II, Chap. 1, pp. 56-57.

54 C. Solterbeck, W. Schattke, J.-W. Zahlmann-Nowitzki, K.-U. Gawlik, L. Kipp, M. Skibowski, C. S. Fadley and M. A. Van Hove, Phys. Rev. Lett. 79, 4681 (1997).